Modeling and Design of a Single Donor/Acceptor Molecule Photodetector Based on Orbital Resonance Using the DFT+NEGF Method

Mohamad Danaie [1*] and Majid Malek[1]

1.Faculty of Electrical and Computer Engineering, Semnan University, Semnan, Iran

*Corresponding author Email: danaie@semnan.ac.ir

***Abstract*-- In this study, we present a photodetector based on molecular donor/acceptor (D/A) interactions utilizing orbital resonance (OR). The device operates by detecting light through interactions between donor and acceptor molecules, resulting in electronic or optical changes. The unique properties of the designed photodetector make it a valuable tool in various fields, including molecular electronics. Initially, molecule optimization and band structure calculations were performed using the density functional theory (DFT) approach to determine the energy and states of the bipartite molecule. Subsequently, the system's Hamiltonian was calculated based on these results. The non-equilibrium Green's function (NEGF) formalism was then employed to model the photodetector using the optimized molecule. We utilized the self-consistent field (SCF) method and optical energy coefficients for modeling. Key photodetector properties such as photocurrent, quantum efficiency (QE), and responsivity (R) were calculated and compared using photons with energies of 1 eV. Next, the current-voltage curve was extracted with and without light exposure. Results indicated negative differential resistance at bias voltages of 2.425 V, 7.54 V, -1.36 V and -6.34 V depending on the input light frequency. The device exhibited a QE=10.2% and an R=0.34 (A/W). Additionally, we modeled the charging effect in the photodetector. Two parameters, quantum and electrostatic capacitance, were proposed to model this effect. Furthermore, the current-voltage curve was displayed considering the charging effect. The designed device also demonstrated the ability to detect and absorb waves at different frequencies.**

***Index Terms*— DFT, D/A molecule, molecular electronics, NEGF, Photodetector.**

I. Introduction

Flexible photodetectors are essential components for the next generation of large-area imagers [1–3] and biomedical sensors [4–8], capable of precision imaging and healthcare monitoring. These wearable applications demand high portability and resilience to frequent deformations, making organic materials particularly promising due to their light weight, mechanical strength, and solution-based fabrication processes [9–12].

Achieving high signal quality under low light intensity is a key goal for organic photodetectors [13–14]. Effective strategies include reducing dark current and increasing photocurrent by incorporating electron/hole (e/h) blocking layers [15], adjusting the thickness and morphology of active layers [16], and transitioning from bulk heterojunction (BHJ) structures to layered donors and acceptors [17].

Optoelectronics has indeed gained significant attention in recent years [18-24]. Single D/A molecule photodetectors have emerged as promising candidates for next-generation optoelectronic devices due to their exceptional sensitivity and unique electronic properties. These photodetectors utilize the quantum mechanical phenomenon of OR to enhance optical response, allowing for miniaturization and performance improvement. The NEGF formalism has proven useful in analyzing and simulating the transport characteristics of these nanoscale devices, providing deep insights into their operating mechanisms [25].

The D/A concept in organic photodetectors is founded on the principles of charge transfer and separation due to light absorption. These pairs can be engineered at the molecular level to optimize electronic and optical properties, leading to efficient photodetection [25]. Recent studies have shown that incorporating OR in these systems significantly enhances sensitivity and selectivity by exploiting quantum tunneling phenomena [26-27]. In organic photodetectors, two basic mechanisms are crucial: (a) the creation of e/h pairs through photon absorption and (b) the separation of carriers to produce contact current and/or voltage. Enhancing these mechanisms is critical for improving optical tracking performance and guiding ongoing research efforts [28]. Our study focuses specifically on the second mechanism—the separation of e–h pairs and subsequent contact current generation.

Recently, a parallel concept has been used to induce negative differential conductance (NDC) in single-molecule junctions. NDC initiation is explained as follows: At zero bias, the energy balance between two sites facilitates resonant charge transfer. Applying a bias voltage disrupts this balance and halts

transmission. Introducing asymmetry into such molecular structures—by adding electron-withdrawing or donating groups on one side—alters the energy balance, creating specific bias points that meet resonance conditions, eliminating asymmetry in current-voltage characteristics, and endowing the molecule with diode-like behavior [29].

The purpose of this paper is to introduce a novel method for contact current generation, differing from the traditional e–h pair separation using electric fields. This new method relies on different transport properties for various carriers, leveraging ORs. In our photodetector, 1,2-bis(4(phenylethynyl)phenyl)-ethane doped with fluorine is used as a channel. Fluorine doping is necessary as it localizes molecular orbitals, requiring the 4-site model [30] and allowing for varied transport properties through ORs.

In this work, we use the DFT+ NEGF method to design a single D/A molecule photodetector based on OR. The NEGF formalism, a powerful computational tool, is widely used to study molecular electronic transfer properties. It provides a comprehensive framework for modeling quantum transport in out-of-equilibrium systems, crucial for understanding single-molecule device behavior under applied bias and illumination [31-32]. By incorporating NEGF formalism in D/A photodetector analysis, researchers can predict current-voltage characteristics, elucidate the role of molecular orbitals, and optimize device performance [33-34].

This paper reviews advances in single D/A molecule photodetectors based on OR, focusing on the insights gained. Our studies contribute to understanding and developing these devices, bridging theoretical and experimental results by modeling charging effects and highlighting outcomes. The structure of this article is as follows: The second section describes the modeling and method. The third section explains the results and discussions. Finally, the fourth section concludes the study.

II. Modeling and Method

Figure 1 illustrates the structure of the studied photodetector. The channel is a molecule consisting of two conjugated parts connected through a non-conjugated linker. This linker allows the molecule to be viewed as two weakly coupled sites in series, where the resonant transition occurs only when the energies of the two sites are equal. The non-conjugated linker is highlighted by a red rectangle in Figure 1. Carbon atoms at the edges are saturated with hydrogen atoms.

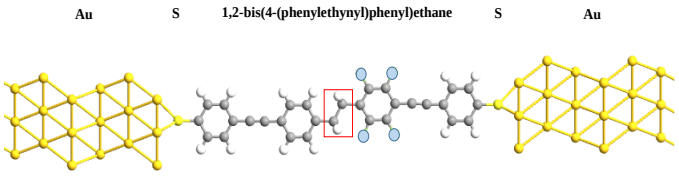

Fig. 1. Atomic structure of the photodetector. The incident light is perpendicular to the channel, with the electric field oriented along the z-direction. The channel length is 26 (Å). The red rectangle indicates the non-conjugated linker of the molecule. Sulfur (S) serves as a bridge between the Au contact and the central molecule.

The source and drain contacts are made of Au to provide negligible contact resistance [35-36]. By substituting fluorine for hydrogen in the right part of the channel, a suitable structure for the 4-site model (see discussion Figure 2) [30] is created. S acts as a connecting bridge between the Au contact and the central molecule, forming strong covalent bonds. This choice ensures stability and high conductivity in electrical connections [29]. It is assumed that monochromatic light with constant power density enters the channel normally and is polarized along the direction of transmission. The NEGF formalism combined with the DFT approach is used to investigate the photodetector's performance, considering charging effects.

The detection mechanism relies on OR. Unlike the Aviram-Ratner rectifier [37-39], which involves vibrationally assisted charge transfer, this method relies on intramolecular coherent resonance transfer [29, 40-41]. In the depicted device (see Figure 2), four energy levels—highest occupied molecular orbital (HOMO), HOMO-1, lowest unoccupied molecular orbital (LUMO), and LUMO+1—play pivotal roles in electron transfer. Conjugated levels significantly influence electron transfer, which does not occur solely from a single level. Electron transfer can occur between two levels via elastic and inelastic pathways, where the energy disparity between levels determines the type of transfer. In elastic transitions, the conjugate pairing of HOMO and HOMO-1, as well as LUMO and LUMO+1 levels, is crucial. When the energy disparity between these conjugate levels is zero, electron transfer occurs. Additionally, the energy disparity between HOMO/LUMO and HOMO-1/LUMO+1 levels should fall within the visible light spectrum, influencing electron excitation and instigating inelastic transitions due to photon absorption. Refer to Figure 8a for the energy level differences and the nature of transitions—elastic and inelastic—during two transmissions.

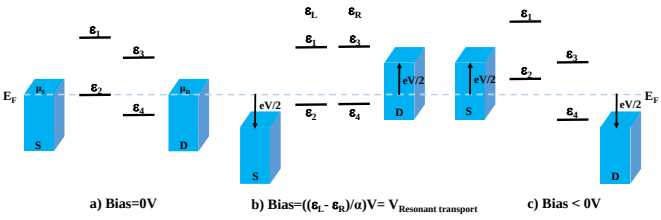

Fig. 2. Four asymmetric levels of the system in a) zero bias voltage, b) resonance bias voltage, and c) reverse bias voltage. ε_1, ε_2, ε_3 and ε_4 represent the energy levels of LUMO+1, HOMO, LUMO and HOMO-1, respectively. S and D indicate source and drain contacts and E_F shows the Fermi level (dashed line).

The structure under investigation utilizes a D-σ-A molecule configuration. As illustrated in Figure 3, the concentration of HOMO and LUMO+1 energy levels is predominantly on the

left section of the molecule. Conversely, HOMO-1 and LUMO energy levels are concentrated in the right segment. This asymmetric distribution results in a structure similar to Figure 2. The positional asymmetry causes the drain contact to interact with the HOMO-1 and LUMO levels, while the source contact engages with the HOMO and LUMO+1 levels. Consequently, direct transitions from the drain contact to the HOMO and LUMO+1 levels, or from the source contact to the HOMO-1 and LUMO levels, do not occur.

This structural arrangement imparts two notable characteristics: First, the asymmetry in energy levels induces a resonant state in the device's current-voltage curve. Second, due to the unequal alignment between the energy levels and the contacts, combined with the electrostatic influence, the orbital energies on the source and drain sides exhibit inverse shifts with changes in bias voltage. This attribute enables the system to accommodate various frequencies, allowing it to detect and absorb waves across different frequencies, effectively functioning as an optical spectrometer [29].

As shown in Figure 2, at zero bias voltage, no molecular energy levels fall within the source and drain electrochemical potential range, preventing charge transport [30]. Under forward bias, as the voltage increases, the energy levels ε_1, ε_2, ε_3 and ε_4 align between the source and drain electrochemical potential thresholds. Charges transport from the source contact to the LUMO+1 and HOMO levels, proceed to the LUMO and HOMO-1 levels, and ultimately reach the drain contact. The asymmetric alignment leads to variations in molecular energy levels, with LUMO and HOMO-1 aligning with the drain contact, while LUMO+1 and HOMO correspond to the source contact. Changes in contact potential induce proportional changes in energy levels [29].

Conversely, under reverse bias, as molecular energy levels align within the source and drain electrochemical potential range, charges transport from the drain contact to the LUMO and HOMO levels, then transition to the LUMO+1 and HOMO levels before reaching the source contact. In summary, the designed photodetector functions as an OR photodetector, where the resonance of molecular energy levels significantly influences charge transport dynamics [30].

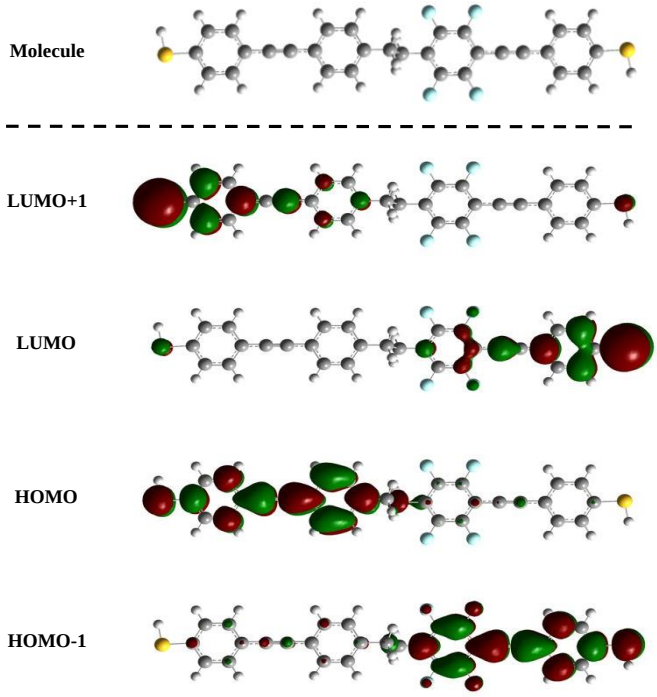

Fig. 3. Molecule (1,2-bis(4-(phenylethynyl)phenyl)ethane) and LUMO+1, LUMO, HOMO, HOMO-1 orbitals of the molecule (at zero bias voltage)

The bias voltage difference applied to source and drain contacts affects the energy difference of the eigenvalues of the levels of the donor and acceptor parts of the molecule in an electrostatic way and is calculated by the following relations:

$$\Delta_{\varepsilon_L,\varepsilon_R} = \sqrt{(aeV)^2 + 2aeV(\varepsilon_L - \varepsilon_R) + (\varepsilon_L - \varepsilon_R)^2 + (2\tau)^2} \quad (1)$$

Here, Δ represents the evolution of the energy gap between ε_L (ε_1 or ε_2) and ε_R (ε_3 or ε_4) with the bias voltage, determining the fraction of the bias voltage that drops inside the molecule [42-43]. α is the portion of the applied bias voltage that changes the energy of the donor and acceptor parts of the molecule through electrostatic phenomena, and τ represents the coupling strengths between the four levels.

Resonance in the absence of light occurs exclusively at bias voltages where the energies of both levels involved in the transition are equal. As this energy difference increases, the coupling decreases, reducing electron transfer from one part to another. Consequently, the current reaches its maximum value at bias voltages where resonance is achieved. To describe and better understand electron transport in the designed structure, we start with the DFT approach and the NEGF formalism [44-45].

A. DFT Simulation

The DFT approach is employed in this paper to find the optimal geometry and calculate the band structure. DFT calculations were performed using the Atomistix ToolKit package (ATK-2018.06) [46] with the following parameters: The exchange-correlation function was investigated using the generalized gradient approximation (GGA) proposed by Perdew, Burke, and Ernzerhof (PBE). We employed the double-ζ plus polarization (DZP) basis set and a kinetic energy cutoff of 150 Ry for numerical calculations. The Brillouin zone is sampled by a 1 × 1 × 150 Monkhorst-Pack grid. The carbon atoms at the edges are saturated with hydrogen atoms. All structures are relaxed until the atomic forces are less than 0.05 eV/Å [47].

B. NEGF

The NEGF formalism is widely used to study the electrical properties of nanoscale devices. Under steady-state conditions, the retarded Green's function is calculated as follows [31, 48]:

$$G(E) = \left[(E + i0^{+})I - H - \sum_1 - \sum_2 - \sum_{ph}\right]^{-1} \quad (2)$$

Here, Σ_1 and Σ_2 are the self-energies of the source and drain contacts, Σ_{ph} is the self-energy of the electron/photon (e/ph) interaction, and H is the channel Hamiltonian in real space. Although calculating NEGF in real space is computationally intensive, it is necessary for achieving more accurate results. The Hamiltonian H of the entire channel is expressed as follows [44]

$$H = H_0 + H_{e-ph} \quad (3)$$

Where $H_\circ$ is the Hamiltonian of the system in the dark mood and is described by the following matrix [43, 49]:

$$H_0 = \begin{bmatrix} \varepsilon_1 - \frac{1}{2}aeV & -\tau & -\tau & -\tau \\ -\tau & \varepsilon_2 - \frac{1}{2}aeV & -\tau & -\tau \\ -\tau & -\tau & \varepsilon_3 + \frac{1}{2}aeV & -\tau \\ -\tau & -\tau & -\tau & \varepsilon_4 + \frac{1}{2}aeV \end{bmatrix} \quad (4)$$

The photon self-energy is calculated from the electromagnetic interaction Hamiltonian. The second quantized interaction Hamiltonian in the presence of a monochromatic photon field which is polarized in the z-direction (direction of channel) [44]:

$$\hat{H}^1 = M_{lm}(\hat{b}e^{-i\omega t} + \hat{b}^{\dagger}e^{i\omega t})\hat{a}_l^{\dagger}\hat{a}_m \quad (5)$$

Which M_{lm} is as follows:

$$M_{lm} = (z_m - z_l)\frac{ie}{\hbar}\left(\frac{\hbar\sqrt{\tilde{\mu}_r\tilde{\epsilon}_r}}{2N\omega\tilde{\epsilon}c}I_\omega\right)^{1/2} l\left|\hat{H}\right|m \quad (6)$$

Where $z_{m/l}$ is the z-axis component of atom position on site m/l. N is the number of photons with energy $\hbar\omega$, and I_ω is the photon flux, defined as the number of photons per unit time per unit area. c represents the speed of light, $\tilde{\epsilon}_r$ denotes the dielectric constant, $\tilde{\mu}_r$ stands for the magnetic permeability coefficient, $\hbar$ represents Planck's reduced constant, and ω depends on the frequency. We assume $P_{op}= 10^7 W/Cm^2$, where $I_\omega=P_{op}/\hbar\omega$. Self-energies of contacts in Eq. (2) are defined by the following relation [44]:

$$\sum_i = V_{LD}^{i\,\dagger} g_L^i V_{LD}^i \qquad i = 1,2 \quad (7)$$

Where V_{LD} is the coupling between the contact and the device, and g_L is Green's function of the isolated semi-infinite contact. Since the coupling is only between the surfaces of the contacts and neighboring sites in the device, only the surface Green's function of the contacts must be computed. In this study, we utilized the Sancho–Rubio iterative scheme [50] to compute this surface Green's function. The in-scattering and out-scattering functions are [43]:

$$\sum_{lm}^{in}(E) = \sum_{pq} M_{lp}M_{qm}\left[NG_{pq}^{n}(E - \hbar\omega) + (N + 1)G_{pq}^{n}(E + \hbar\omega)\right] \quad (8a)$$

$$\sum_{lm}^{out}(E) = \sum_{pq} M_{lp}M_{qm}\left[NG_{pq}^{p}(E + \hbar\omega) + (N + 1)G_{pq}^{p}(E - \hbar\omega)\right] \quad (8b)$$

Where G^n and G^p are the electron and hole correlation functions, respectively. Finally, the last expression for the e/ph self-energy is computed as:

$$\Gamma_{ph}(E) = \sum_{lm}^{in}(E) + \sum_{lm}^{out}(E) \quad (9a)$$

$$\sum_{ph} = -(i/2)\Gamma_{ph} \quad (9b)$$

The real part of the self-energy (R_{ph}) in the above relation is neglected, since it does not change the photon absorption/ emission rate and only shifts energy up to few meV [51]. The electron and hole correlation functions including the effects of e/ph interactions are as follows [52]:

$$G^n(E) = G(E)\left[\Gamma_1(E)f_1(E) + \Gamma_2(E)f_2(E) + \sum_{lm}^{in}(E)\right]G(E)^{\dagger} \quad (10a)$$

$$G^p(E) = G(E)[\Gamma_1(E)(1 - f_1(E)) + \Gamma_2(E)(1 - f_2(E)) + \sum_{lm}^{out}(E)]G(E)^{\dagger} \quad (10b)$$

Where $\Gamma_{1,2}=i(\Sigma_{1,2}-\Sigma_{1,2}\dagger)$ is the broadening function of the source/drain contact and $f_{1,2}$ is the source/drain Fermi function shown by the following relation:

$$f_{L,R} = \left[1 + exp\left(\varepsilon - \frac{\mu_{L,R}}{K_B T}\right)\right]^{-1} \quad (11)$$

Where K_B is Boltzmann's constant, T is the temperature and $\mu_{L,R}$ represents the source/drain contact electrochemical potential.

After calculating the self-energy matrix the photocurrent can be calculated by considering the scattering due to photons ($\sum_{ph}^{out}$ and $\sum_{ph}^{in}$) in G^n and G^p. However, the dark current [53-55], which refers to the current of the device in the absence of incident photon radiation, is calculated by ignoring the $\sum_{ph}^{out}$ and $\sum_{ph}^{in}$ terms in G^n and G^p [56]:

$$I_{L,R} = Trace\left[\sum_{L,R}^{n} A\right] - Trace\left[\Gamma_{L,R} G^n\right] \quad (12)$$

When $A = i\left[G - G^\dagger\right]$, the Eq. (12) can also be expressed as follows:

$$I_{L,R} = \frac{2e}{\hbar} \int \frac{dE}{2\pi} \left(f_L(E) - f_R(E)\right) T(E) \quad (13)$$

The electron transmission, denoted as T(E), is described as follows:

$$T(E) = Tr\{\Gamma_L G(E) \Gamma_R G^\dagger(E)\} \quad (14)$$

The dependence of the retarded Green's function (G) on the Green's functions (G^n /G^p), and vice versa, as observed in Eqs. (10a) and (10b), necessitates the use of the self-consistent Born loop until convergence. After the initial calculation of the G, G^n, A and G^p functions in the dark mode, we obtain the functions by subjecting the system to light. This process is repeated until the optical interactions are fully calculated, continuing until each iteration matches the previous one. Finally, using the achieved convergence and the computed values for Green's functions, it becomes possible to calculate the photocurrent from Eq. (13).

Two crucial parameters required for investigating the performance of the organic photodetectors are their QE and R. These parameters are defined by the following relations [57]:

$$QE = \frac{I_{ph}/q}{P_{op}/\hbar\omega} \quad (15)$$

And

$$R = \frac{I_{ph}}{P_{op}} \quad (16)$$

It is important to note that the current-voltage characteristic is strongly affected by the potential and must be accounted for even in the simplest model. If the channel is isolated, then Laplace's equation can be solved to calculate the potential ($\in_r$ is the relative permittivity that can change spatially) [58]:

$$\nabla.(\varepsilon_r \nabla V) = 0 \quad (17)$$

This can be visualized using the capacitor circuit model under favorable boundary conditions. The potential energy in the channel is obtained by multiplying the electrostatic potential (V) by the electron charge ($-q$) [31, 57-58]:

$$U_L = \frac{C_S}{C_{ES}}(-qV_S) + \frac{C_D}{C_{ES}}(-qV_D) \quad (18)$$

Where C_S and C_D are the source and drain capacitances at a distance z from the source, respectively. C_{ES} is called electrostatic capacitance and is defined as follows:

$$C_{ES} = C_S + C_D \quad (19)$$

In this regard, the index L means that the potential is obtained from the solution of the Laplace equation and any changes in the electric charge are ignored. Otherwise, there is a change $\Delta\rho$ in the value of the electron density in the channel, requiring the solution of the following Poisson equation [31, 57-58]:

$$\nabla.(\varepsilon_r \nabla V) = \frac{-\Delta\rho}{\varepsilon_0} \quad (20)$$

Where

$$\rho(E) = -\frac{1}{\pi} ImTrG(E) \quad (21)$$

To clarify the capacitor model, we will consider the combination of a molecule and a contact. In the absence of a bias voltage, the contact and isolated molecule are at the same potential. Therefore, their vacuum energy (the potential energy of a free electron) in isolation is the same. When contact is made with the molecule, equilibrium must be established in the combined system. To prevent current from flowing, there must be a uniform Fermi energy in both the contact and the molecule. But if the Fermi energies in the contact and isolated molecules are different, how is equilibrium achieved?

Since Fermi levels change with the addition or subtraction of charge, equilibrium is achieved by charge transfer between the contact and the molecule. Charge transfer changes the contact potential relative to the molecule and shifts the relative vacuum energies. This is known as "charging." Charge transfer also affects Fermi levels because electrons fill some states and empty others. Both charging and state-filling effects can be modeled by capacitors. First, we consider the filling of the electronic state [59].

When the contact and molecule bond, charge flows to align the filling levels. However, a molecule does not necessarily have a

uniform density of states (DOS), and only a fraction of the charge may be transferred. In general, the number of charges on the molecule can be determined using [31, 59]:

$$n = \int_{-\infty}^{+\infty} D(E) f(E, E_F) dE \quad (22)$$

Where $D(E) = \frac{[A(E)]}{2\pi}$ is the DOS per unit of energy. For small energy changes, we can linearize this to determine the effect of charge transfer on E_F. We are interested in dE_F/dn. For degenerate systems, we can simplify the Eq. (22):

$$n = \int_{-\infty}^{E_F} D(E) dE \quad (23)$$

Taking the derivative concerning energy gives:

$$\frac{dn}{dE_F} = D(E_F) \quad (24)$$

Rearranging, we get:

$$\delta E_F = \frac{\delta n}{D(E_F)} \quad (25)$$

Therefore, after charge transfer, the Fermi energy inside the molecule changes by $\delta n/D$.

Sometimes it is convenient to model the effect of filling the DOS with a "quantum capacitance," which is defined as [31, 59]:

$$C_Q = q^2 D(E_F) \quad (26)$$

i.e

$$\delta E_F = \frac{q^2}{C_Q} \delta n \quad (27)$$

If the molecule has a high DOS at the Fermi level, its quantum capacitance is high, and more charge must be transferred to move the Fermi level [31, 59].

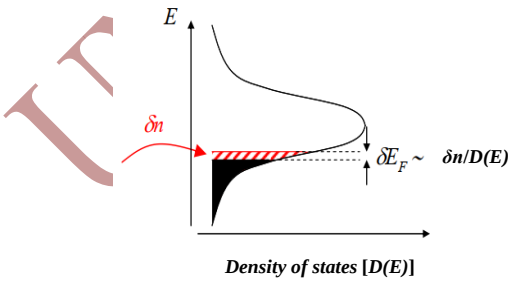

Fig. 4. Charge transfer changes the Fermi level in a conductor. The magnitude of the change is determined by the DOS at the Fermi level and is often expressed in terms of "quantum capacitance."

The charge flowing from the contact to the molecule creates a potential across the quantum capacitance. Note that this is a change in the Fermi level, not an electrostatic potential. It is also important to note that the quantum capacitance usually depends on the Fermi level in the molecule [31, 59].

Electrons are charged. Therefore, electron transfer from a contact to a molecule leaves a net positive charge on the contact and a net negative charge on the molecule. This charge at the interface changes the potential of the molecule relative to the contact, akin to moving the entire water reservoir up and down. The charge helps balance and reduces the number of electrons transferred after contact is made.

The contact and molecule can be considered as two plates of a capacitor. This capacitance is called C_{ES} (electrostatic capacitance) to distinguish it from the quantum capacitance discussed previously. When the charge is transferred across the interface, the capacitor is charged, a voltage is established, and the molecule's potential changes. The change in the potential of the molecule for each electron transferred is known as charge energy and is reflected in the change in vacuum energy. From the basic relation for a capacitor [31, 59]:

$$C_{ES} = \frac{Q}{V} \quad (28)$$

Where V is the voltage across the capacitor. We can calculate the potential change due to the charging:

$$U_C = qV = \frac{q^2}{C_{ES}} \delta n \quad (29)$$

We will see that δn is a dynamic quantity (it changes as the current flows). This can be very important in nanodevices because the electrostatic capacitance is very small. The charging effect on the molecule is related to the application of a voltage across a surface capacitor, changing the potential of the molecule. As a result, the vacuum level is displaced at the location of the molecule, displacing all molecular states with it. Additionally, the transferred charge fills some previously empty states in the molecule. Summarizing these effects, we find that the Fermi energy of the neutral molecule (E_{F0}) is related to the Fermi energy of the contact-molecule combination (E_F), and both effects change the Fermi energy in the molecule [31, 59].

$$E_F = \delta n/D + \frac{q^2}{C_{ES}} \delta n + E_F^0 \quad (30)$$

In terms of quantum capacitance:

$$E_F = \frac{q^2}{C_Q} \delta n + \frac{q^2}{C_{ES}} \delta n + E_F^0 \quad (31)$$

We model the potential change effect by strongly shifting all energy levels within the molecule [31, 59].

$$D \rightarrow D(E-U) \tag{32}$$

We can extend the model to two-terminal devices.

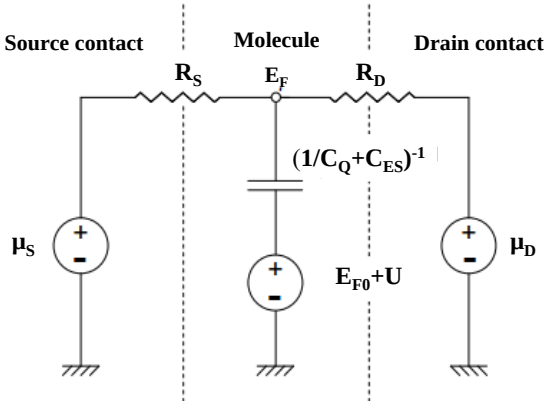

Fig. 5. A small signal model for a source/molecule/drain two-terminal circuit.

n and I are rewritten below, taking into account charging effects:

$$n = \int_{-\infty}^{+\infty} D(E-U) f(E,E_F) dE \tag{33a}$$

$$I_{L,R} = Trace\left[\Sigma_{L,R}^{n} A(E-U)\right] - Trace\left[\Gamma_{L,R} G^{n}(E)\right] \tag{33b}$$

The net potential change in the molecule is determined by the sum of the Laplace potential and an additional term that is proportional to the change in the number of electrons [31, 59]:

$$U = U_L + U_c = U_L + \frac{q^2}{C_{ES}} \Delta n \tag{34}$$

The constant $U_\circ = q^2/C_{ES}$ represents the change in potential energy per additional electron, called the single-electron charge energy. The change Δn in the number of electrons is calculated based on the reference number of electrons ($n_\circ$) which are initially in the channel and have a known energy level.

The problem with current evaluation is that it depends on U and therefore n. But Eq. (33a) is not a closed-form solution for n, because the right-hand side also depends on n through U. Except in simple cases, this means we must iteratively solve for n and then use the solution to obtain I. Therefore, to solve the Eq. (33b), the SCF method is needed. As shown in Figure 6, this method continues until convergence. The value of U in each step is obtained from the following relation [31, 59]:

$$U = U_\circ + \eta[U - U_\circ] \tag{21}$$

Where η is a positive number (typically less than 1) chosen as large as possible so that the results do not diverge (which appears as increasing U-U_0 from one iteration to the next).

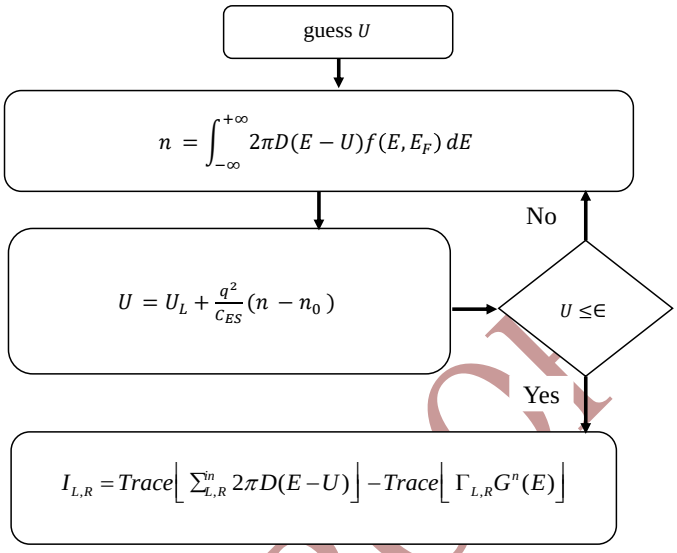

Fig. 6. SCF algorithm to calculate the current considering the charging effect.

III. Results and Discussions

In this section, we aim to examine the outcomes derived from simulating the molecular device through DFT + NEGF method.

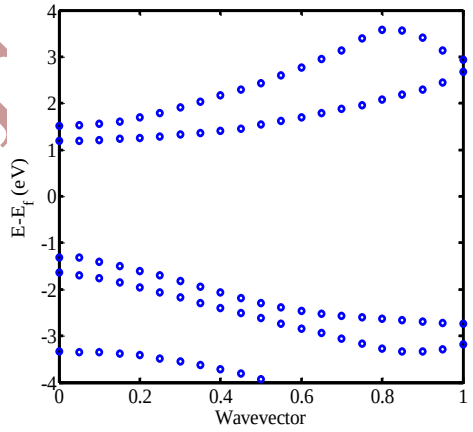

Fig. 7. Band structure of designed structure calculated by DFT approach.

Figure 7 shows the band structure calculated via the DFT approach, revealing HOMO, LUMO, LUMO+1, and HOMO-1 energy levels with corresponding energies of -5.61, -3.11, -2.78, and -5.94 eV, respectively and this results are listed in Table 1. Each orbital within the examined molecule is predominantly concentrated within either the right or left segment of the molecule.

Transmission was calculated by coupling S atoms to Au contacts [60- 61] with a coupling strength of -0.05 eV. A bias voltage was applied by introducing a uniform electric field along the axis connecting the S atoms to the molecule.

Table I
Energy and spatial average of molecular orbitals

Level	Energy (eV)	Coordinate Mean (A°)
LUMO+1	-2.78	-6.5
LUMO	-3.11	6.5
HOMO	-5.61	6.5
HOMO-1	-5.94	-6.5

The coupling strengths between the HOMO-1 and HOMO levels are stipulated as -0.01 eV, and between the LUMO and LUMO+1 levels as -0.01 eV. Moreover, the positioning of the HOMO, LUMO, LUMO+1, and HOMO-1 orbitals is presumed at the center of each respective section of the molecule (considering the molecule's two distinct parts), situated at -6.5, 6.5, -6.5, and 6.5 Angstroms, measured from the average location of carbon atoms along the z-axis direction in each segment of the molecule for every localized molecule within each part. The coordinate center is set as the molecule's center along the z-axis direction.

Based on these specific data and obtained results, the Hamiltonian matrix of the system, absent of light and at a temperature of zero Kelvin, can be expressed as follows:

$$H_0 = \begin{bmatrix} -3.055 & -0.01 & -0.01 & -0.01 \\ -0.01 & -5.885 & -0.01 & -0.01 \\ -0.01 & -0.01 & -2.835 & -0.01 \\ -0.01 & -0.01 & -0.01 & -5.665 \end{bmatrix} \quad (43)$$

Where the Hamiltonian dependence of the system on the applied bias voltage can be seen. Also, in the Hamiltonian matrix, α is equal to 0.55 [42]. According to the Eq. (6), the matrix in the case of light radiation to the system can be written as follows:

$$M_{lm} = \begin{bmatrix} 0 & 0 & t & t \\ 0 & 0 & t & t \\ -t & -t & 0 & 0 \\ -t & -t & 0 & 0 \end{bmatrix} \quad (44)$$

The coupling of the molecule with the contacts at different energies is assumed to be constant, which is known as the wideband limit (WBL) model. Based on this, the coupling matrices of molecular levels and contact are considered as follows [29]:

$$\Gamma_R = \begin{bmatrix} 0 & 0 & 0 & 0 \\ 0 & 0 & 0 & 0 \\ 0 & 0 & 0.05 & 0 \\ 0 & 0 & 0 & 0.05 \end{bmatrix}$$

$$\Sigma_R = \begin{bmatrix} 0 & 0 & 0 & 0 \\ 0 & 0 & 0 & 0 \\ 0 & 0 & -0.025i & 0 \\ 0 & 0 & 0 & -0.025i \end{bmatrix} \quad (45)$$

And also:

$$\Gamma_L = \begin{bmatrix} 0.05 & 0 & 0 & 0 \\ 0 & 0.05 & 0 & 0 \\ 0 & 0 & 0 & 0 \\ 0 & 0 & 0 & 0 \end{bmatrix}$$

$$\Sigma_L = \begin{bmatrix} -0.025i & 0 & 0 & 0 \\ 0 & -0.025i & 0 & 0 \\ 0 & 0 & 0 & 0 \\ 0 & 0 & 0 & 0 \end{bmatrix} \quad (46)$$

In Figure 8c, the current-voltage curve of the system is simulated under conditions without light radiation, revealing distinct peaks occurring at bias voltages of 0.6, 5.74, and -4.54 volts. These peaks materialize when molecular alignments synchronize, inducing resonance. A comparative analysis between the current-voltage curve of the device (Figure 8c), the energy levels of the molecule concerning bias voltage (Figure 8a), and the difference curve of the Hamiltonian eigenvalues of the device concerning bias voltage (depicted in Figure 8b) elucidates that current amplification transpires at bias voltages where the energy disparity among molecule levels reaches zero. The difference between the eigenvalues of the corresponding energy levels at resonant bias voltages notably diminishes to its minimum value. In essence, during this resonance, the associated orbitals become energized and propagate across the molecule. As spatial states extend throughout the molecule and orbital energies intersect, the likelihood of electron transition from one side of the molecule to the other—facilitating electron transfer between levels—escalates, leading to enhanced current flow at resonant bias voltages.

In Figure 8b, each peak corresponds to the resonance and alignment of two orbitals. For instance, at 0.6 V, the current arises solely from the alignment of the HOMO-1/HOMO and LUMO+1/LUMO energy levels, where electron passage occurs exclusively through these orbitals. At 5.74 V, current generation emanates from the alignment of LUMO+1 and HOMO-1 levels, while at -4.54 V, electron passage and current flow are instigated by the alignment of the HOMO and LUMO orbitals. A crucial aspect reflected in these curves is the discrepancy observed at 0.6 V concerning the maximum current compared to the peaks at 5.74 V and -4.54 V. At 0.6 V, although the resonance of two pairs of energy levels contributes to the current generation, it is noteworthy that for optimum current, the pair of levels should be fully accessible to the contacts.

However, the LUMO+1 pair with LUMO isn't entirely accessible to the contacts due to energy level broadening induced by the contact/molecule coupling, restricting only a portion of the levels' accessibility to the contacts.

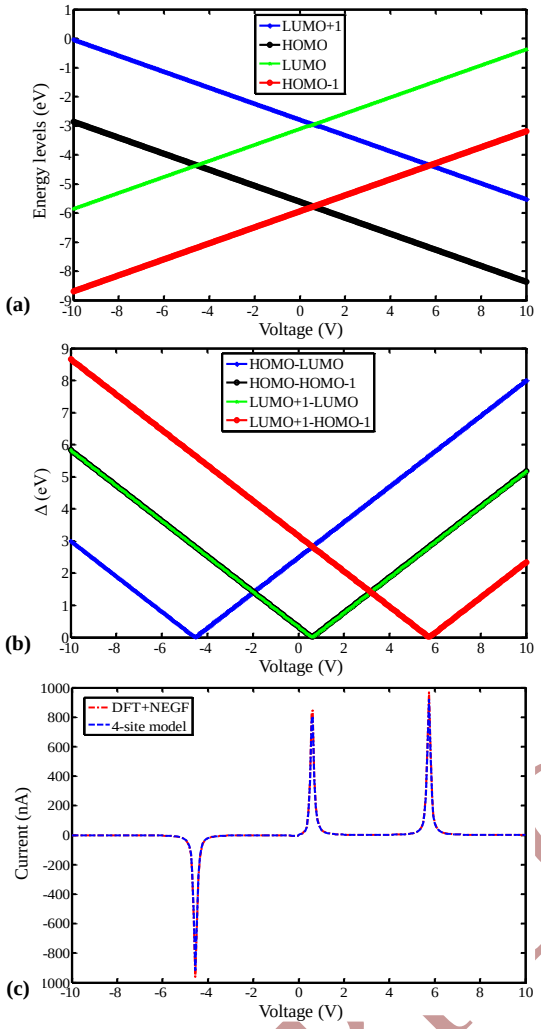

Fig 8. a) Energy changes of molecular orbitals according to bias voltage. b) The difference of eigenvalues of pairs of energy levels according to bias voltage. c) Current-voltage curve calculated using DFT + NEGF (dashed-dotted red, Γ=0.09 (eV)) and using the 4-site model (dashed blue, Γ=0.05 (eV)) in the absence of light.

The curves presented in Figure 9 illustrate the DOS at varying bias voltages (0.6, 5.74 and -4.54 volts), highlighting the impact of energy level availability within the molecule on electron transfer and the generation of system current. At 0.6 V, all four energy levels exhibit resonance conditions, yet only the HOMO-1/HOMO pair is accessible to the contacts. Similarly, at 5.74 V, the HOMO-1/LUMO+1 pairs satisfy the mentioned conditions, facilitating electron passage from one side source contact to the opposing side drain contact. At -4.54 V, the depiction reveals the accessibility of HOMO, LUMO, and HOMO-1 levels to the contacts. However, only the HOMO/LUMO pair contributes to electron transfer. This is due to the necessity for both the availability of energy levels and the occurrence of resonance—essential for electron transfer across the molecule. At -4.54 V, these conditions are only met for the HOMO/LUMO pair, while the HOMO-1 and LUMO+1 levels fail to meet either of these conditions. This delineates the critical role played by the simultaneous fulfillment of resonance conditions and the accessibility of energy levels to contact interfaces for effective electron transfer in the system.

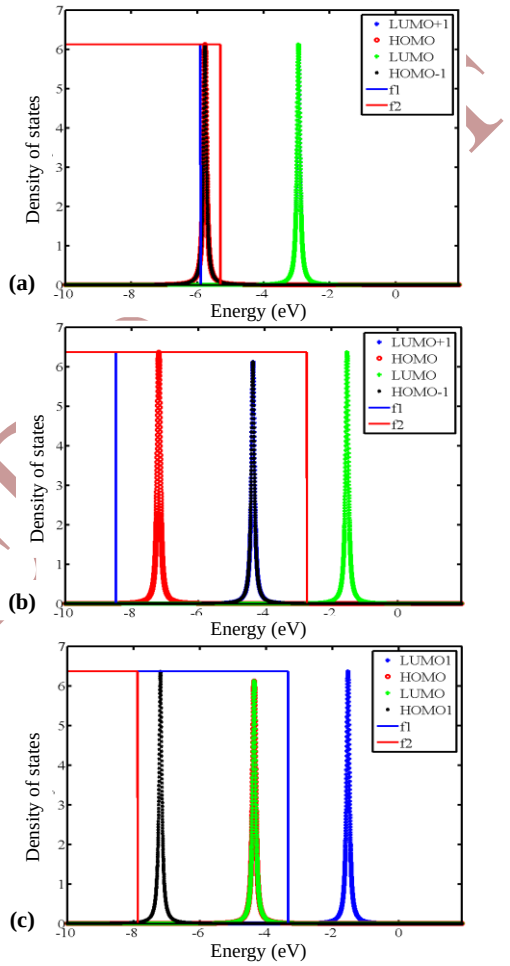

Fig. 9. DOS at bias voltages a) 0.6 (V), b) 5.74 (V), c) -4.54 (V). f_1 and f_2 represent the Fermi-Dirac distribution function for source and drain contacts.

In Figure 10, the transmission curves of the device are depicted for various bias voltages. The graphical representation illustrates that the transfer of electrons from one contact to another occurs specifically at energies where the paired levels are accessible to the contacts. This observation underlines the correlation between the availability of specific energy level pairs and the facilitation of electron transfer between the contacts in the system.

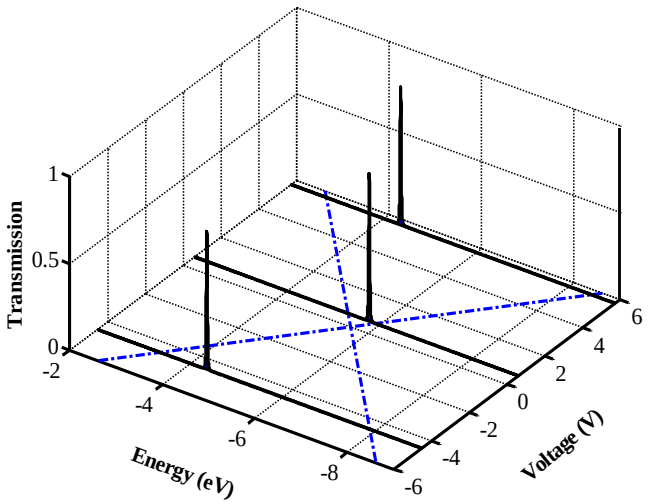

Fig. 10. Transmission curve in terms of device energy in bias voltages a) 0.6 (V), b) 5.74 (V), c) -4.54 (V). The blue dotted line represents the Dirac Fermi distribution functions that express the bias window.

The bias window refers to the energy range that is affected by the applied bias voltage and affects the behavior of energy levels of the donor and acceptor parts. Figure 11 shows R and QE calculated from Eqs 15 and 16.

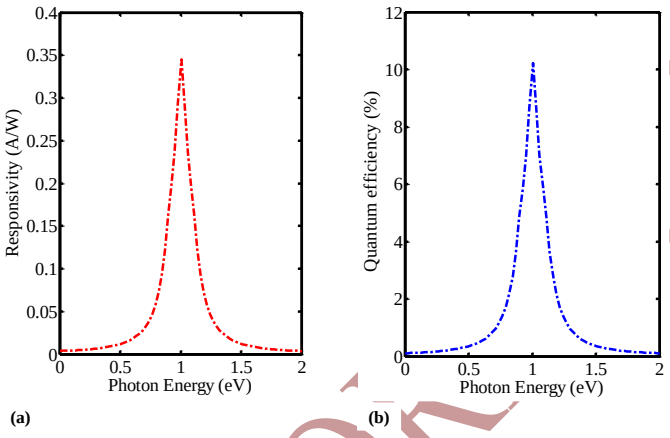

Fig. 11. a) R and b) QE of the designed photodetector versus the incident photon energy 1 (eV), under an externally applied bias of 5.74 (V)

This value represents the ratio of the output current to the input optical power and the ratio of absorbed photons to generated electrons, which are 0.34 and 10.2%, respectively.

Figure 12 shows the effect of single-wavelength light entering the system compared to its absence on the current-voltage curve (dashed line in both Figures). The current-voltage curve, shown without light irradiation, undergoes detectable changes when exposed to light with a photon energy of 1 eV. When the energy difference between the molecular surfaces aligns with the energy of the incident light, electron transport becomes inelastic, resulting in additional peaks in the current-voltage curve. This inelastic transition, under the influence of the frequency and intensity of the irradiated light, completes the existing peaks of the elastic transition within the system. The interference and effectiveness of elastic transmission among inelastic transmission are acceptable phenomena. As a result, the current-voltage curve of the device exhibits characteristics similar to that of an optical transistor, producing peaks that are attributed to the frequency and intensity of the irradiated light. Notably, the peaks labeled P1, P2, P3, and P4 originate from radiative light absorption and enhance electron transfer from low energy levels to higher levels. Simultaneously, three additional peaks appear at different bias voltages due to elastic transition. Inelastic transmission peaks are realized when the energy difference between two molecular surfaces, each of which is located on separate sides of the molecule and does not interfere, falls within the energy range of the photon radiation.

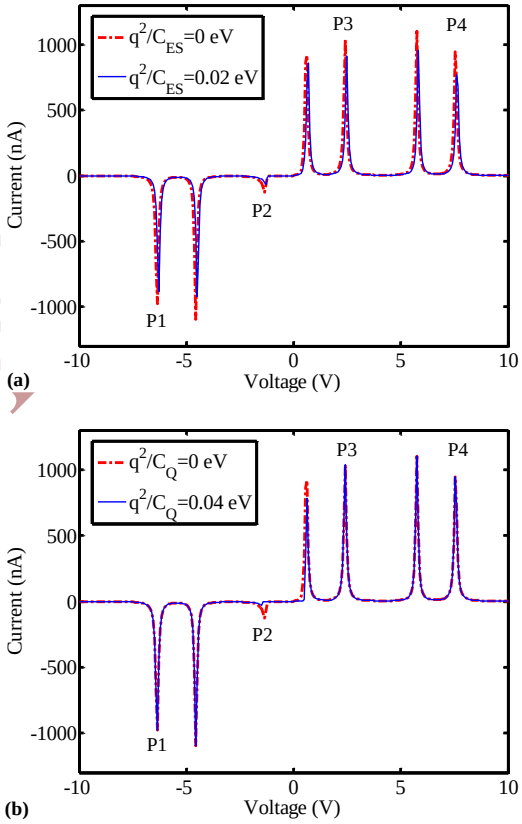

Fig. 12. Current peaks caused by single-frequency light with a photon energy of 1 (eV) (dashed line). (a) Electrostatic effect caused by charging with q^2/C_{ES} =0.02 (eV) (solid line). (b) The effect of state filling caused by charging with q^2/C_Q =0.04 (eV) (solid line).

Determining the exact current-voltage characteristics of a molecular device requires calculating the potential following the algorithm in Figure 6, using a SCF approach. Assuming the molecule is grounded, electrostatic effects change the source and drain potentials and only charging changes the molecular energy level. Figures 12a and 12b show the difference between the current-voltage curves with the charging effect and without the charging effect on the molecule. Figure 12a shows the electrostatic effect caused by charging on current peaks with and without light (solid line). In positive bias, the greatest effect

is on the current peaks without light, while in negative bias, the greatest effect is on the peaks with light, leading to a decrease in current. Figure 12b illustrates the state-filling effect of charging-induced on current peaks with and without light (solid line). As mentioned earlier, this effect only alters the Fermi energy of the molecule. The change in Fermi energy significantly affects the current-voltage curve due to the unavailability of energy levels at low bias voltages (both positive and negative).

The curve of the DOS of the system after absorbing a photon with an energy of 1 eV is shown in Figure 13 which leads to the transfer of electrons if the energy difference between the pair of molecular levels is equal to 1 eV. Also, these curves show the necessity of the availability of source and drain electrochemical potentials of the energy levels, which these conditions are met at 2.425, 7.54, -1.36 and -6.34 volts.

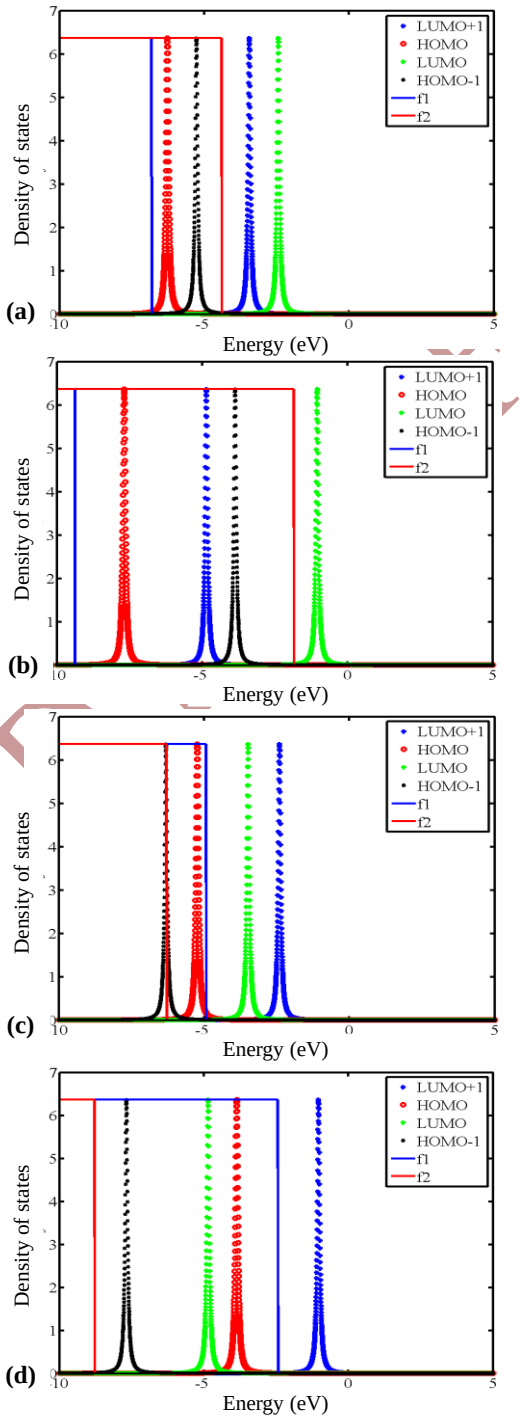

Fig. 13. DOS diagram in bias voltages a) 2.425 (V), b) 7.54 (V), c) -1.36 (V) and d) -6.34 (V). f_1 and f_2 represent the Fermi-Dirac distribution function for source and drain contacts.

At 2.425 V, the levels accessibility curve shows HOMO/HOMO-1 to contacts that this pairs with a level difference of 1 eV contribute to electron transfer. At 7.54 V, this condition is satisfied only for the HOMO-1/LUMO+1 pair. Whereas, at -1.36 V and -6.34, the HOMO/HOMO-1 and HOMO/LUMO pairs satisfy the mentioned conditions and facilitate the electron transfer from one side to the opposite side, respectively.

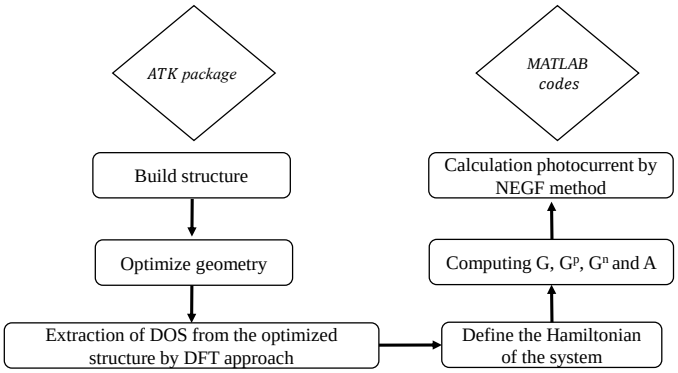

Fig. 14. The flowchart of basic overview of the steps involved in using ATK and MATLAB for computational simulations.

Finally, Figure 14 provides a flowchart illustrating the computational workflow, which involves utilizing ATK for structure optimization and electronic structure calculations, followed by data extraction and subsequent analysis and visualization in MATLAB.

IV. Conclusion

In this article, we describe the modeling and simulation of a single D/A molecule photodetector based on OR using the DFT+NEGF method. We demonstrate that this device operates by detecting light through interactions between the donor and acceptor parts of the molecule, leading to electronic or optical changes.

Initially, molecule optimization and band structure calculations were performed using the DFT approach with the Atomistix ToolKit package (ATK-2018.06) to determine the energy and states of the bipartite molecule. Subsequently, the Hamiltonian of the system was calculated based on these results. The NEGF formalism in MATLAB was then used to model the photodetector with the optimized molecule. We employed the SCF method and optical self-energy coefficients for modeling. Key properties of the photodetector, such as photocurrent, QE, and R, were calculated and compared using photons with an energy of 1 eV.

Next, current-voltage curves were extracted with and without light exposure. The results showed negative differential resistance at bias voltages of 2.425 V, 7.54 V, -1.36 V and -6.34 V, depending on the frequency of the input light. The device exhibited a QE of 10.2% and an R of 0.34 (A/W). Additionally, we modeled the effect of charging on the photodetector. Two parameters, quantum and electrostatic capacitance, were calculated to model this effect. The current-voltage curve, considering the charging effect, was displayed, showing the current reduction due to charging. Furthermore, the designed device demonstrated the ability to detect and absorb waves at different frequencies.

NOMENCLATURE

The highest occupied molecular orbital	$HOMO$
The lowest unoccupied molecular orbital	$LUMO$
Transmission	$T(E)$
Retarded Green's function	$G(E)$
Fermi-Dirac distribution function	$f(E)$
Number of photons	N
Electron charge	q
Contact/molecule coupling	Γ
Density of state	$DOS(E)$
Electrochemical potential	μ
Boltzmann's constant	K_B
Potential	U

V. References

[1]Ko, Heung Cho, Mark P Stoykovich, Jizhou Song, Viktor Malyarchuk, Won Mook Choi, Chang-Jae Yu, Joseph B Geddes Iii, Jianliang Xiao, Shuodao Wang and Yonggang Huang. "A Hemispherical Electronic Eye Camera Based on Compressible Silicon Optoelectronics." Nature 454, no. 7205 (2008): 748-753.

[2]Goossens, Stijn, Gabriele Navickaite, Carles Monasterio, Shuchi Gupta, Juan José Piqueras, Raúl Pérez, Gregory Burwell, Ivan Nikitskiy, Tania Lasanta and Teresa Galán. "Broadband Image Sensor Array Based on Graphene–Cmos Integration." Nature Photonics 11, no. 6 (2017): 366-371.

[3]Pierre, Adrien, Abhinav Gaikwad, and Ana Claudia Arias. "Charge-Integrating Organic Heterojunction Phototransistors for Wide-Dynamic-Range Image Sensors." Nature Photonics 11, no. 3 (2017): 193-199.

[4]Lochner, Claire M, Yasser Khan, Adrien Pierre and Ana C Arias. "All-Organic Optoelectronic Sensor for Pulse Oximetry." Nature communications 5, no. 1 (2014): 5745.

[5]Yakunin, Sergii, Mykhailo Sytnyk, Dominik Kriegner, Shreetu Shrestha, Moses Richter, Gebhard J Matt, Hamed Azimi, Christoph J Brabec, Julian Stangl and Maksym V Kovalenko. "Detection of X-Ray Photons by Solution-Processed Lead Halide Perovskites." Nature Photonics 9, no. 7 (2015): 444-449.

[6]Büchele, Patric, Moses Richter, Sandro F Tedde, Gebhard J Matt, Genesis N Ankah, Rene Fischer, Markus Biele, Wilhelm Metzger, Samuele Lilliu and Oier Bikondoa. "X-Ray Imaging with Scintillator-Sensitized Hybrid Organic Photodetectors." Nature Photonics 9, no. 12 (2015): 843-848.

[7] Suzuki, D, S Oda and Y Kawano. "A Flexible and Wearable Terahertz Scanner." Nature Photonics 10, no. 12 (2016): 809-813.

[8]Yokota, T, P Zalar, M Kaltenbrunner, H Jinno, N Matsuhisa, H Kitanosako, Y Tachibana, W Yukita, M Koizumi and T Someya. "Vol. 2, Pp. E1501856." Sci. Adv, (2016).

[9]Jiang, Zhi, Kenjiro Fukuda, Xiaomin Xu, Sungjun Park, Daishi Inoue, Hanbit Jin, Masahiko Saito, Itaru Osaka, Kazuo Takimiya and Takao Someya. "Reverse-Offset Printed Ultrathin Ag Mesh for Robust Conformal Transparent Electrodes for High-Performance Organic Photovoltaics." Advanced Materials 30, no. 26 (2018): 1707526.

[10] Jiang, Zhi, Kenjiro Fukuda, Wenchao Huang, Sungjun Park, Roda Nur, Md Osman Goni Nayeem, Kilho Yu, Daishi Inoue, Masahiko Saito and Hiroki Kimura. "Durable Ultraflexible Organic Photovoltaics with Novel Metal-Oxide-Free Cathode." Advanced Functional Materials 29, no. 6 (2019): 1808378.

[11] Wang, Sihong, Jie Xu, Weichen Wang, Ging-Ji Nathan Wang, Reza Rastak, Francisco Molina-Lopez, Jong Won Chung, Simiao Niu, Vivian R Feig and Jeffery Lopez. "Skin Electronics from Scalable Fabrication of an Intrinsically Stretchable Transistor Array." Nature 555, no. 7694 (2018): 83-88.

[12] Kaltenbrunner, Martin, Tsuyoshi Sekitani, Jonathan Reeder, Tomoyuki Yokota, Kazunori Kuribara, Takeyoshi Tokuhara, Michael

Drack, Reinhard Schwödiauer, Ingrid Graz and Simona Bauer-Gogonea. "An Ultra-Lightweight Design for Imperceptible Plastic Electronics." Nature 499, no. 7459 (2013): 458-463.
[13] Pierre, Adrien and Ana Claudia Arias. "Solution-Processed Image Sensors on Flexible Substrates." Flexible and Printed Electronics 1, no. 4 (2016): 043001.
[14] Simone, Giulio, Matthew J Dyson, Stefan CJ Meskers, René AJ Janssen and Gerwin H Gelinck. "Organic Photodetectors and Their Application in Large Area and Flexible Image Sensors: The Role of Dark Current." Advanced Functional Materials 30, no. 20 (2020): 1904205.
[15] Saracco, Emeline, Benjamin Bouthinon, Jean-Marie Verilhac, Caroline Celle, Nicolas Chevalier, Denis Mariolle, Olivier Dhez and Jean-Pierre Simonato. "Work Function Tuning for High-Performance Solution-Processed Organic Photodetectors with Inverted Structure." Adv. Mater 25, no. 45 (2013): 6534-6538.
[16] Keivanidis, Panagiotis E, Peter KH Ho, Richard H Friend and Neil C Greenham. "The Dependence of Device Dark Current on the Active-Layer Morphology of Solution-Processed Organic Photodetectors." Advanced Functional Materials 20, no. 22 (2010): 3895-3903.
[17] Xiong, Sixing, Lingliang Li, Fei Qin, Lin Mao, Bangwu Luo, Youyu Jiang, Zaifang Li, Jinsong Huang and Yinhua Zhou. "Universal Strategy to Reduce Noise Current for Sensitive Organic Photodetectors." ACS Applied Materials & Interfaces 9, no. 10 (2017): 9176-9183.
[18] Mohammadi, Ghader, Ali Asghar Orouji and Mohammad Danaie. "A Tunable Narrow Single-Mode Bandpass Filter Using Graphene Nanoribbons for Thz Applications," Scientific Reports 14, no. 1 (2024): 21217.
[19] Danaee, Ebrahim, Alireza Geravand and Mohammad Danaie. "Wide-Band Low Cross-Talk Photonic Crystal Waveguide Intersections Using Self-Collimation Phenomenon." Optics Communications 431, (2019): 216-228.
[20] Khani, Shiva, Mohammad Danaie and Pejman Rezaei. "Compact and Low-Power All-Optical Surface Plasmon Switches with Isolated Pump and Data Waveguides and a Rectangular Cavity Containing Nano-Silver Strips." Superlattices and Microstructures 141, (2020): 106481.
[21] Danaie, Mohammad and Hassan Kaatuzian. "Bandwidth Improvement for a Photonic Crystal Optical Y-Splitter." Journal of the Optical Society of Korea 15, no. 3 (2011): 283-288.
[22] Mohammadi, Ghader, Aliasghar Orouji and Mohammad Danaie. "Highly Compact Tunable Hourglass-Shaped Graphene Band-Stop Filter at Terahertz Frequencies." Results in Optics 13, (2023): 100575.
[23] Rahmani, Komeil, Saeed Mohammadi and Mohammad Danaie. "Analytical Investigation on the Electro-Optical Characteristics of White Graphene." Journal of Computational Electronics 20, no. 5 (2021): 1860-1867.
[24] Khalili, Sajjad and Mohammad Danaie. "Interface Analysis of Indium Antimonide and Passive Layer in Infrared Detector and Presenting a New Structure to Improve Dark Current." Superlattices and Microstructures 120, (2018): 796-805.
[25] Siqueira, MRS, SM Corrêa, RM Gester, J Del Nero and AMJC Neto. "Single-Molecular Diodes Based on Opioid Derivatives." Journal of Molecular Modeling 21, (2015): 1-9.
[26] Ren, Hao, Jing-De Chen, Yan-Qing Li and Jian-Xin Tang. "Recent Progress in Organic Photodetectors and Their Applications." Advanced Science 8, no. 1 (2021): 2002418.
[27] Zhu, Danlei, Wei Jiang, Zetong Ma, Jiajing Feng, Xiuqin Zhan, Cheng Lu, Jie Liu, Jie Liu, Yuanyuan Hu and Dong Wang. "Organic Donor-Acceptor Heterojunctions for High-Performance Circularly Polarized Light Detection." Nature communications 13, no. 1 (2022): 3454.
[28] Zarei, MH and MJ Sharifi. "Defect-Based Graphene Nanoribbon Photodetectors: A Numerical Study." Journal of Applied Physics 119, no. 21 (2016).
[29] Perrin, Mickael L, Elena Galan, Rienk Eelkema, Ferdinand Grozema, Joseph M Thijssen and Herre SJ Van Der Zant. "Single-Molecule Resonant Tunneling Diode." The Journal of Physical Chemistry C 119, no. 10 (2015): 5697-5702.
[30] Perrin, Mickael L, Matthijs Doelman, Rienk Eelkema and Herre SJ Van Der Zant. "Design of an Efficient Coherent Multi-Site Single-Molecule Rectifier." Physical Chemistry Chemical Physics 19, no. 43 (2017): 29187-29194.
[31] Datta, Supriyo. Quantum Transport: Atom to Transistor: Cambridge University Press, 2005.
[32] Taylor, Jeremy, Hong Guo and Jian Wang. "Ab Initio Modeling of Open Systems: Charge Transfer, Electron Conduction, and Molecular Switching of a C 60 Device." Physical Review B 63, no. 12 (2001): 121104.
[33] Cohen, Guy and Michael Galperin. "Green's Function Methods for Single Molecule Junctions." The Journal of Chemical Physics 152, no. 9 (2020).
[34] Ho Choi, Seong, BongSoo Kim and C Daniel Frisbie. "Electrical Resistance of Long Conjugated Molecular Wires." Science 320, no. 5882 (2008): 1482-1486.
[35] Saha, Atanu K, Gobinda Saha and ABM Harun-ur Rashid. "Graphene Nanoribbon Quantum-Well Interband and Intersubband Photodetector." IEEE Transactions on Electron Devices 62, no. 12 (2015): 4082-4090.
[36] Shahnooshi, Farzaneh, Ali A Orouji and Abdollah Abbasi. "Enhanced Performance of Graphene/Algaas/Gaas Heterostructure Schottky Solar Cell Using Algaas Drainage." Journal of Materials Science: Materials in Electronics 33, no. 7 (2022): 4617-4627.
[37] Aviram, Arieh and Mark A Ratner. "Molecular Rectifiers." Chemical Physics Letters 29, no. 2 (1974): 277-283.
[38] Gupta, Ritu, Jerry A. Fereiro, Akhtar Bayat, Anurag Pritam, Michael Zharnikov and Prakash Chandra Mondal. "Nanoscale Molecular Rectifiers." Nature Reviews Chemistry 7, no. 2 (2023): 106-122.
[39] Chen, Lichuan, Zixian Yang, Qichao Lin, Xiaohui Li, Jie Bai and Wenjing Hong. "Evolution of Single-Molecule Electronic Interfaces." Langmuir 40, no. 4 (2024): 1988-2004.
[40] Howarth, Ashlee J, Yangyang Liu, Peng Li, Zhanyong Li, Timothy C Wang, Joseph T Hupp and Omar K Farha. "Chemical, Thermal and Mechanical Stabilities of Metal-Organic Frameworks." Nature Reviews Materials 1, no. 3 (2016): 1-15.
[41] Liu, Junjie and Dvira Segal. "Generalized Input-Output Method to Quantum Transport Junctions. Ii. Applications." Physical Review B 101, no. 15 (2020): 155407.
[42] Hnid, Imen, Ali Yassin, Imane Arbouch, David Guérin, Colin Van Dyck, Lionel Sanguinet, Stéphane Lenfant, Jérôme Cornil, Philippe Blanchard and Dominique Vuillaume. "Molecular Junctions for Terahertz Switches and Detectors." Nano Letters 24, no. 8 (2024): 2553-2560.
[43] Malek, Majid and Mohammad Danaie. "Design of N-Doped C60-Σ-B-Doped C60 Photodetector Based on Resonant Tunneling Diode Using DFT and NEGF Method." Journal of Molecular Modeling 30, no. 11 (2024): 366.
[44] Henrickson, Lindor E. "Nonequilibrium Photocurrent Modeling in Resonant Tunneling Photodetectors." Journal of Applied Physics 91, no. 10 (2002): 6273-6281.
[45] Mahler, Günter and Rainer Wawer. "Quantum Networks: Dynamics of Open Nanostructures." VLSI Design 8, no. 1-4 (1998): 191-196.
[46] Quantumatk Version O-2018.06, Synopsys Quantumatk. (https://www.synopsys.
com/silicon/quantumatk.html).
[47] Golzani, Mozhgan, Mohammad Poliki and Saeed Haji-Nasiri. "Γ-Graphyne Rectifier and Ndr Tunable by Doping, Line Edge Roughness and Twist." Computational Materials Science 190, (2021): 110303.
[48] Zarei, Mohammad H and Mohammad J Sharifi. "Asymmetric Lateral Graphene/H-Bcn Heterojunctions: A New Method for Separation of Carriers in Graphene Nanoribbon Photodetectors." Superlattices and Microstructures 122, (2018): 522-529.
[49] Malek, Majid and Mohammad Danaie. "A Single Molecule Diode Based on Gold Electrodes and Benzene Molecule: Conductivity

and Coupling Analysis." Journal of Molecular Modeling 29, no. 11 (2023): 332.
[50] Sancho, MP Lopez, JM Lopez Sancho, JM Lopez Sancho and J Rubio. "Highly Convergent Schemes for the Calculation of Bulk and Surface Green Functions." Journal of Physics F: Metal Physics 15, no. 4 (1985): 851.
[51] Gao, Qun and Jing Guo. "Quantum Mechanical Simulation of Graphene Photodetectors." Journal of Applied Physics 112, no. 8 (2012).
[52] Anantram, MP, Mark S Lundstrom and Dmitri E Nikonov. "Modeling of Nanoscale Devices." Proceedings of the IEEE 96, no. 9 (2008): 1511-1550.
[53] Madadi, Dariush, Iman Gharibshahian and Ali A Orouji. "High-Performance A-Fapbi3 Perovskite Solar Cells with an Optimized Interface Energy Band Alignment by a Zn (O, S) Electron Transport Layer." Journal of Materials Science: Materials in Electronics 34, no. 1 (2023): 51.
[54] Sharafi, Foad, Ali A Orouji and Mohammad Soroosh. "A Novel Field Effect Photodiode to Control the Output Photocurrent and Fast Optical Switching." Optical and Quantum Electronics 54, no. 3 (2022): 171.
[55] Shahnazarisani, Hadi and Ali Asghar Orouji. "A Novel Soi Mesfet by Implanted N Layer (Inl-Soi) for High Performance Applications." Modeling and Simulation in Electrical and Electronics Engineering 1, no. 1 (2021): 7-12.
[56] Rudi, Somayeh Gholami, Rahim Faez, Mohammad Kazem Moravvej-Farshi, and Kamyar Saghafi. "Effect of Stone-Wales defect on an armchair graphene nanoribbon-based photodetector." Superlattices and Microstructures 130, (2019): 127-138.
[57] Datta, Supriyo. "Electrical resistance: an atomistic view." Nanotechnology 15, no. 7 (2004): S433.
[58] Garrigues, Alvar R., Li Yuan, Lejia Wang, Eduardo R. Mucciolo, Damien Thompon, Enrique Del Barco, and Christian A. Nijhuis. "A single-level tunnel model to account for electrical transport through single molecule-and self-assembled monolayer-based junctions." Scientific Reports 6, no. 1 (2016): 26517.
[59] Zahid, Ferdows, Magnus Paulsson and Supriyo Datta. "Electrical Conduction through Molecules." In Advanced Semiconductor and Organic Nano-Techniques, 1-41: Elsevier, 2003.
[60] Perrin, Mickael L, Riccardo Frisenda, Max Koole, Johannes S Seldenthuis, Jose A Celis Gil, Hennie Valkenier, Jan C Hummelen, Nicolas Renaud, Ferdinand C Grozema and Joseph M Thijssen. "Large Negative Differential Conductance in Single-Molecule Break Junctions." Nature Nanotechnology 9, no. 10 (2014): 830-834.
[61] Verzijl, CJO, JS Seldenthuis and JM Thijssen. "Applicability of the Wide-Band Limit in Dft-Based Molecular Transport Calculations." The Journal of Chemical Physics 138, no. 9 (2013).